Closed-orbit theory for photodetachment in a time-dependent electric field

B. C. Yang and F. Robicheaux*

Department of Physics and Astronomy, Purdue University, West Lafayette, Indiana 47907, USA

(Received 14 March 2016; published 17 May 2016)

The standard closed-orbit theory is extended for the photodetachment of negative ions in a time-dependent electric field. The time-dependent photodetachment rate is specifically studied in the presence of a single-cycle terahertz pulse, based on exact quantum simulations and semiclassical analysis. We find that the photodetachment rate is unaffected by a weak terahertz field, but oscillates complicatedly when the terahertz pulse gets strong enough. Three types of closed classical orbits are identified for the photoelectron motion in a strong single-cycle terahertz pulse, and their connections with the oscillatory photodetachment rate are established quantitatively by generalizing the standard closed-orbit theory to a time-dependent form. By comparing the negative hydrogen and fluorine ions, both the in-phase and antiphase oscillations can be observed, depending on a simple geometry of the contributed closed classical orbits. On account of its generality, the presented theory provides an intuitive understanding from a time-dependent viewpoint for the photodetachment dynamics driven by an external electric field oscillating at low frequency.

DOI: 10.1103/PhysRevA.93.053413

I. INTRODUCTION

Quantum effects from closed (or periodic) classical orbits in a microscopic system have been explored in many different branches of physics [1]. One of the most typical processes in atomic and molecular physics is the photoionization of neutral atoms or the photodetachment of negative ions in external fields [2]. Its studies often promise an intuitive picture of the embedded dynamics, which not only reveals an interesting correspondence between classical and quantum mechanics, but also allows a better control and manipulation on a microscopic scale. The general physical picture and formalism are known as closed-orbit theory [3–5], which has been applied or extended in different situations. However, almost all the systems investigated before are time independent and therefore energy conserving [6–15]. Time-dependent systems have been rarely studied, with the one exception being the photoionization of neutral atoms in a static electric field plus a weak oscillating field [16,17]. In this paper, we demonstrate an application of closed-orbit theory for the photodetachment of negative ions in a time-dependent electric field.

Many kinds of specific field profiles, such as a microwave field or a low-frequency laser pulse, could be applied to study the time-dependent effect of an external field on the photodetachment rate of negative ions. Recently, a strong single-cycle terahertz (THz) pulse has been available in a table-top experiment. As a result of its simplicity and other peculiarities, the single-cycle THz pulse has been applied in exploring the ionization dynamics of Rydberg atoms [18–20], as well as controlling the alignment and orientation of polar molecules [21,22]. Inspired in part by these results, we consider the possibility of using a single-cycle THz field to manipulate the photodetachment dynamics of negative ions. Temporal interferences in the time-dependent electron flux (or the angle-resolved energy spectrum) at large distances were investigated in a previous paper [23] by extending the original idea for traditional photodetachment microscopy in a static electric field [24–27]. The classical trajectory of the photoelectron was tracked from the negative-ion center to a large distance. We found that some trajectories could return to the source region when the single-cycle pulse is strong enough. This observation of closed classical orbits constitutes the main motivation of this work.

Following the general picture depicted by closed-orbit theory [3–5], an external field can modulate the photon absorption rate in the photoionization and photodetachment processes by driving back an outgoing electron wave to the source region where the initial bound state is localized. The returning electron wave interferes with the outgoing wave near the source center. Each closed classical orbit corresponds to one sinusoidal term in the total modulation function. Therefore, an oscillatory photodetachment rate should be expected if the applied single-cycle THz pulse is strong enough that the electron can be driven back to the source region. This is indeed observed in our quantum simulations for a strong THz pulse. In Fig. 1, a representative case is shown for the negative hydrogen ion (H^-). It can be observed that the photodetachment rate is quite stable in a weak THz pulse with the maximum field strength $F_m = 10$ kV/cm, but oscillates in a complex way when a stronger THz pulse is used such as $F_m = 40$ kV/cm. By examining the classical trajectories, no closed orbit is found for $F_m = 10$ kV/cm, while three different types of closed orbits are found when $F_m = 40$ kV/cm. These observations are qualitatively consistent with the general predictions of closed-orbit theory. To quantitatively understand the oscillatory behavior as in Fig. 1(b), we have to generalize the existing formulas to include time-dependent field effects. It turns out that the generalized formulas agree very well with exact quantum simulations.

Comparing with the well-established closed-orbit theory for the photodetachment dynamics in a static electric field [14,15], the generalized formulas mainly have two differences as follows. (a) A static electric field can always guarantee one and only one closed orbit, and the oscillation phases are opposite between the photodetachment rates from an s-wave source such as negative fluorine ion (F^-) and a p-wave source such as H^-. While in a time-dependent electric field

*robichf@purdue.edu

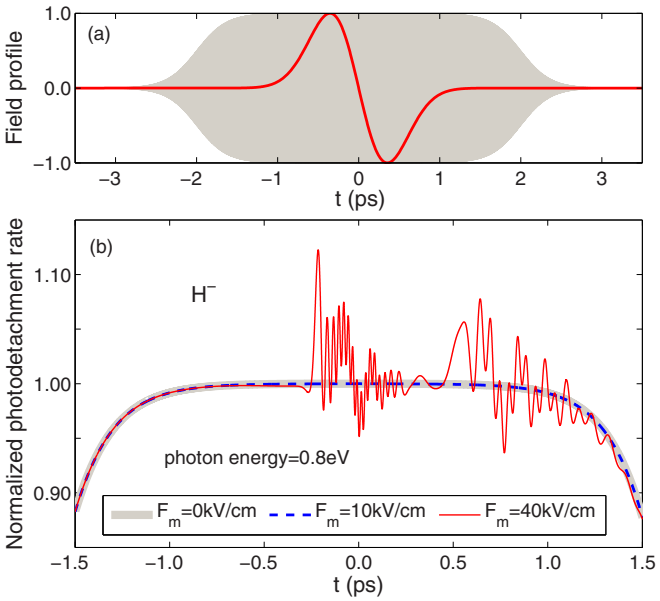

FIG. 1. (a) Field configurations reproduced from Ref. [23] with a slight modification. The gray curve and the solid red line represent the weak laser field and the single-cycle THz pulse, respectively, divided by their corresponding field amplitudes. The laser-field oscillation cannot be resolved due to its high frequency. (b) Time-dependent photodetachment rate obtained from exact quantum simulations for H^-. The THz pulse strengths F_m are given in the legend for different lines, respectively. All of the curves are normalized using the value of the photodetachment rate at $t = 0$ ps without the single-cycle pulse applied ($F_m = 0$ kV/cm).

no closed orbit exists if the maximum momentum transfer is not large enough, more than one closed orbit may be found if the field is strong. Determined by a simple property of each closed orbit, both the in-phase and antiphase oscillations can be observed by comparing the time-dependent photodetachment rates of H^- and F^-. (b) An electron's kinetic energy is conserved if it was driven back to the ion by a static field. In contrast, when the electron is driven back by a time-dependent electric field, its kinetic energy is usually different from its initial value. Consequently, each sinusoidal term in the total modulation function is multiplied by an additional coefficient related to both the electron's outgoing and returning momenta along the corresponding closed classical orbit.

Although the single-cycle THz pulses are specifically studied, the presented theory is quite general. The related formulas can be used directly for the photodetachment of negative ions in any other forms of the time-dependent electric field, as long as the whole photodetachment process can be divided approximately into two steps: one-photon absorption from a weak laser field followed by the photoelectron motion in the applied external field. The only additional work needed for a specific system is to identify all of the possible closed classical orbits. We note that an experiment has been done for the photodetachment of negative chlorine ions in a microwave field [28,29], and several theoretical studies have also been reported [29–31]. However, all of the previous time-dependent treatments assumed the applied field varied slowly enough so that the electron was driven by a constant electric field during each detachment event, which approximately corresponds to the situation in the reported experiment [28,29]. In this sense, our current work provides further insight into the general cases of a time-dependent electric field.

In the following section, the theoretical model with a specific single-cycle THz pulse is briefly summarized, as well as the numerical method we used for quantum simulations. The three types of closed classical orbits are identified in Sec. III, and their corresponding returning waves are specified in Sec. IV. The general formulas for the time-dependent photodetachment rate are presented in Sec. V by extending the standard closed-orbit theory for the photodetachment of negative ions in a static electric field. Some calculations and discussions are presented in Sec. VI, followed by a brief conclusion in Sec. VII. Atomic units are used throughout this work unless specified otherwise.

II. THEORETICAL MODEL AND NUMERICAL APPROACH

We choose to study the photodetachment of negative ions (H^- and F^-) in a single-cycle THz pulse as a specific system, based on several simple reasons as introduced above. Most importantly, this system has almost all the essential elements expected for the other general cases, which can be seen clearly in the following sections. In addition, a numerical solution of Schrödinger's equation is also possible as long as the single-cycle pulse strength is not extremely large as in Fig. 1(b), which allows us to examine the accuracy of closed-orbit theory.

The details of the theoretical model have been described in Ref. [23]. Here, we give a brief summary and present the necessary equations related to our present work. We assume that the weak laser field and the applied single-cycle THz pulse are both linearly polarized along the z axis. The influence of the THz pulse is negligible on the initial ground state of the negative ion. The much higher frequency of the laser field relative to the THz pulse allows the whole photodetachment process to be approximated as two successive steps: the weakly bound electron in a short-range potential well is first released by absorbing one photon from the weak laser field, and then the photoelectron motion after escaping from the atom center is mainly guided by the single-cycle THz pulse.

As in our previous paper [23], we restrict the weak laser field within a finite width as in Fig. 1(a). The specific envelope function has the following form:

$$f_L(t) = \frac{1}{2}\left[\tanh\left(\frac{t-t_u}{t_L}\right) - \tanh\left(\frac{t-t_d}{t_L}\right)\right], \qquad (1)$$

where $t_d = -t_u = 4t_w$ with t_w denoting the single-cycle pulse duration in Eq. (3) below. The parameter t_L is selected to be large enough so that the possible acceleration and deceleration effects are negligible in the outgoing electron wave when the field envelope is ramping on and off. For example, the photon energy $\hbar\omega_L$ used for H^- is 0.8 eV in Fig. 1(b), and $t_L = 80T_0$ with T_0 approximately 4.6 fs after the convention in Ref. [23]. For F^-, the weak laser-field frequency is chosen to give the same electron kinetic energy E_0 as for H^-, allowing us to examine effects caused by the different angular distributions of the initially outgoing electron waves. For those laser parameters listed above, the generated outgoing wave at

each initial time t_i can be written as

$$\psi_0(r,\theta_i,\phi_i,t_i) = f_L(t_i)\psi_{\rm out}(r,\theta_i,\phi_i)e^{-iE_0t_i}, \tag{2}$$

with its amplitude approximately following the laser-field envelope, where $(r,\ \theta_i,\ \phi_i)$ denote spherical coordinates of the electron relative to the rest atom. The spatial function $\psi_{\rm out}(r,\theta_i,\phi_i)$ corresponds to the time-independent outgoing wave generated by a cw laser.

The applied single-cycle THz pulse is assumed to have a Gaussian-shape vector potential,

$$A(t) = -\frac{F_m t_w}{\sqrt{2}} e^{-\frac{t^2}{t_w^2}+\frac{1}{2}}, \tag{3}$$

which gives a time-dependent single-cycle electric field as in Fig. 1(a) with $F(t) = -dA(t)/dt$. $t_w = 0.5$ ps in Fig. 1, and its value may be changed for the other calculations. Both the quantum propagation approach and the semiclassical propagation scheme have been described in Ref. [23] for the evolution of the generated electron wave driven by a single-cycle THz pulse. For a sufficiently strong THz pulse as in Fig. 1(b), an exact quantum simulation is possible. The details can be found in Ref. [23], and the basic idea is to solve the following inhomogeneous Schrödinger equation:

$$\left\{i\frac{\partial}{\partial t} - [H_a + H_F(t) - E_0]\right\}\widetilde{\Psi}(\mathbf{r},t) = f_L(t)D\varphi_i, \tag{4}$$

on a two-dimensional space spanned by the discretized radial points and angular momentum basis with different l values. The source term on the right-hand side of Eq. (4) comes from the interaction of negative ions with a weak laser field, where D and φ_i represent, respectively, the dipole operator and the initial bound state of negative ions. The atomic Hamiltonian $[\mathbf{p}^2/2 + V(r)]$ and the interaction term $[F(t)z]$ with a single-cycle THz pulse are denoted, respectively, by H_a and $H_F(t)$ on the left-hand side of Eq. (4). The specific forms of the binding potential $V(r)$ for H^- and F^- are taken from Refs. [32] and [33], respectively. The corresponding binding energies E_b are 0.02773 and 0.125116 a.u. for H^- and F^-, respectively, by diagonalizing the atomic Hamiltonian matrix in a large radial box.

The wave function $\widetilde{\Psi}(\mathbf{r},t)$ in Eq. (4) multiplied by a phase term $\exp(-iE_0t)$ is the detached-electron wave function at each time instant with a single-cycle THz pulse applied. Therefore, the time-dependent photodetachment rate $\Upsilon(t)$ can be calculated as [17]

$$\Upsilon(t) = \frac{d}{dt}\int \widetilde{\Psi}^*(\mathbf{r},t)\widetilde{\Psi}(\mathbf{r},t)d^3\mathbf{r}. \tag{5}$$

In practice, we found that quantum simulations for $\Upsilon(t)$ can be done efficiently in a smaller radial box than that in Ref. [23] by using a mask function $M(r > r_c) = 1 - \alpha[(r - r_c)/(r_m - r_c)]^2\delta t$ to absorb the wave-function part approaching a large distance after each time step δt. The calculation of $\Upsilon(t)$ is done in each time step before the wave function $\widetilde{\Psi}(\mathbf{r},t)$ multiplied by the mask function. The absorbing strength α, the beginning point r_c of the mask function, and the radial box boundary r_m should be adjusted carefully to make the numerical results convergent. For our calculations in this work, we consistently use $\alpha = 0.005$. The appropriate values of r_c and r_m can be chosen by referring to the classical turning points of the possible closed orbits discussed in the following section. For instance, $r_c = 6500$ a.u. and $r_m = 8000$ a.u. for Fig. 1(b) with $F_m = 40$ kV/cm. For $F_m = 0$ and $F_m = 10$ kV/cm in Fig. 1(b), we did not use the mask function.

III. CLOSED CLASSICAL ORBIT

For our purpose here, we need to find all the possible closed classical orbits returning back to the atom center. The electron orbit equation has been obtained as [23]

$$\rho(t) = k_0(t - t_i)\sin(\theta_i), \tag{6}$$

$$z(t) = [k_0\cos(\theta_i) - A(t_i)](t - t_i) + \int_{t_i}^{t} A(t')dt', \tag{7}$$

in the cylindrical coordinates (ρ, z) with the atom center at the origin, where $k_0 = \sqrt{2E_0}$. By setting $\rho(t) = 0$ and $z(t) = 0$, we get the following condition for the possible closed orbits:

$$[k_0\cos(\theta_i) - A(t_i)](t - t_i) = -\int_{t_i}^{t} A(t')dt', \tag{8}$$

with $\theta_i = 0$ or π. This criteria can be expressed geometrically as in Fig. 2(a), where the rectangular area below the horizontal dashed line and the shaded area below the reversed vector-potential curve $[-A(t_i)]$ are, respectively, the left- and right-hand sides of Eq. (8). The solution to Eq. (8) requires an equivalent of these two areas. Note that the crossings between the horizontal dashed line and the reversed vector-potential curve correspond to the spatial turning points $[p_z(t) = 0]$ of each trajectory, and their corresponding time is

$$t_<^0 = -t_>^0 = -t_w\sqrt{\ln\left[\frac{A_m}{A(t_i) - k_0}\right]} \tag{9}$$

for $\theta_i = 0$, and

$$t_>^\pi = t_w\sqrt{\ln\left[\frac{A_m}{A(t_i) + k_0}\right]} \tag{10}$$

for $\theta_i = \pi$, with $A_m = -F_m t_w \exp(1/2)/\sqrt{2}$ denoting the amplitude of the vector potential in Eq. (3).

After a simple geometric analysis in Fig. 2, we can easily determine the possible range of the starting and returning time for each closed orbit. In Figs. 2(a) and 2(c) for $\theta_i = 0$, the horizontal dashed line must cross the reversed vector-potential curve, which requires

$$|A(t_i) - A_m| > k_0 \ \text{ and } \ t_i < 0 \ \text{ if } \ \theta_i = 0. \tag{11}$$

Therefore, the starting time t_i of the possible closed orbit must be negative and less than $-t_w\sqrt{\ln[A_m/(A_m + k_0)]}$. The corresponding two returning time instants $t_{\rm ret01}$ and $t_{\rm ret02}$ satisfy $t_<^0 < t_{\rm ret01} \leqslant t_>^0$ and $t_{\rm ret02} \geqslant t_>^0$, respectively. In addition, the position of the second turning point $z(t_>^0)$ cannot be positive for the trajectory returning back. In Figs. 2(e) and 2(g) for $\theta_i = \pi$, the same argument related to the crossing as for $\theta_i = 0$ leads to

$$-A(t_i) - k_0 > 0 \ \text{ and } \ |A(t) - A_m| > k_0 \ \text{ if } \theta_i = \pi. \tag{12}$$

Accordingly, only the classical trajectories starting between $-t_w\sqrt{\ln(-A_m/k_0)}$ and $t_w\sqrt{\ln(-A_m/k_0)}$ can be driven back

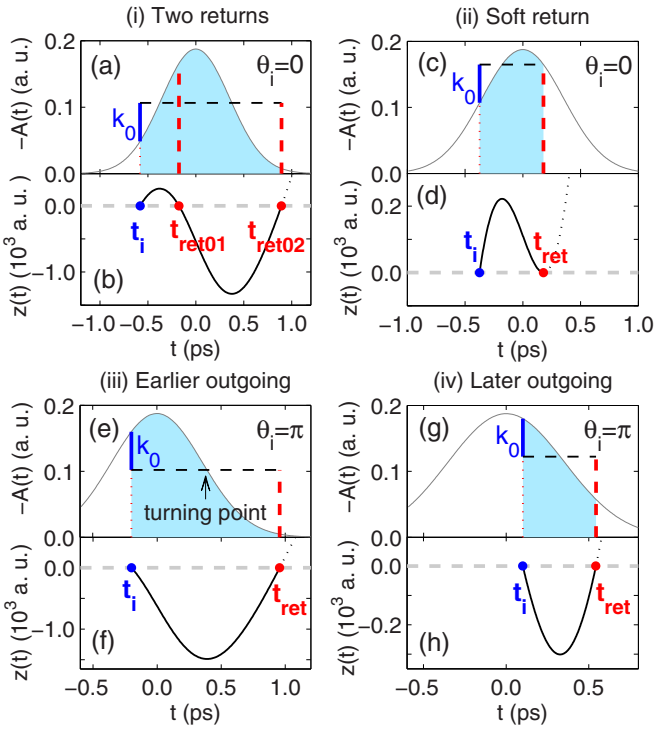

FIG. 2. Graphic demonstration of the possible closed classical orbits in a strong single-cycle THz pulse. The specific case in Fig. 1(b) for $F_m = 40$ kV/cm is used as an example. Panels (i) and (ii) are two possible cases for $\theta_i = 0$, and (iii) and (iv) are two possible cases for $\theta_i = \pi$. In each panel, the top subplot is a geometric expression of Eq. (8) and the bottom one shows the corresponding trajectory. For each trajectory, the position of the vertical bold solid (blue) line indicates the starting time, while the vertical bold dashed (red) lines locate its returning time. Both the starting and returning time instants are marked accordingly along each closed orbit (solid curve) in (b), (d), (f), and (h), where the horizontal bold dashed line shows the ion-center location, with the dotted line representing the continuation of each trajectory.

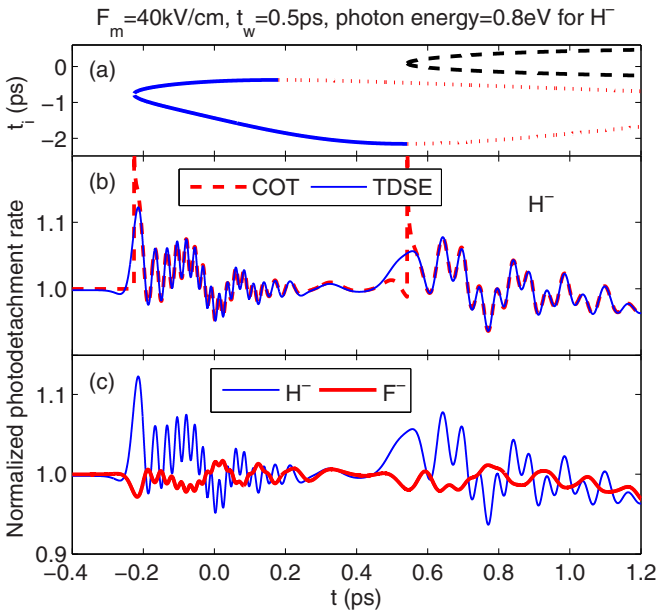

FIG. 3. (a) Returning time plot for the relevant closed orbits in Figs. 1(b) and 2, giving the initial, outgoing time t_i for each possible closed orbit returning back to the atom center at time t. The three types of closed orbits are identified in order by the solid blue curve, the dotted lines, and the dashed lines. (b) Time-dependent photodetachment rate for H^-. The bold dashed curve is given by Eqs. (35)–(37) from closed-orbit theory (COT), while the solid blue curve is from exact quantum simulations by directly solving the time-dependent Schrödinger equation (TDSE) in Eq. (4). (c) Comparison between the photodetachment rates for H^- (thin blue curve) and F^- (bold red line) obtained from quantum simulations. All of the quantum results have been normalized using the value of the photodetachment rate at $t = 0$ ps without any external fields applied.

to the source region. The returning time must be positive and larger than $t_w\sqrt{\ln[A_m/(A_m + k_0)]}$. Furthermore, the returning time should also be later than the time of the turning point.

For each closed orbit, the exact starting and returning time can be found numerically according to Eq. (8). Figure 3(a) shows the starting time of each closed orbit as a function of the corresponding returning instant with $F_m = 40$ kV/cm. To be clear, we have categorized all the possible closed orbits into three types according to their outgoing angle and returning direction. The first type of closed orbit starts with $\theta_i = 0$ and goes back with $\theta_{\rm ret} = \pi$, which includes the first-time returned trajectory in Figs. 2(a) and 2(b) and the special case shown in Figs. 2(c) and 2(d). The second-time returned trajectory as in Figs. 2(a) and 2(b) is the second type of closed orbit with $\theta_i = \theta_{\rm ret} = 0$. The other two cases depicted in Figs. 2(e)–2(h) correspond to the third type of closed orbit with $\theta_i = \pi$ and $\theta_{\rm ret} = 0$. These three types of closed orbits are distinguished in Fig. 3(a) by the blue solid curve and the red dotted and black dashed lines, respectively. The joint point between the blue solid curve and the red dotted line in Fig. 3(a) represents a special situation, as demonstrated in Figs. 2(c) and 2(d), which we call a soft return after Refs. [34,35]. In this case, the atom-center location is just a turning point of the electron trajectory, and $p_z = 0$ when the electron returns back to the atom center.

IV. SEMICLASSICAL RETURNING WAVE

For an electron propagating along each classical trajectory, the corresponding quantum wave can be constructed approximately in a semiclassical way. To obtain the semiclassical returning wave, we first choose an initial spherical surface of radius R centered at the negative ion. As in the standard procedure [5,14], the small radius R is selected near the atom center such that the initially outgoing wave is already asymptotic but not obviously distorted by external fields. Accordingly, the time-independent function $\psi_{\rm out}(R,\theta_i,\phi_i)$ in Eq. (2) has the following spherically outgoing wave form [26]:

$$\psi_{\rm out}(R,\theta_i,\phi_i) = C(k_0)Y_{lm}(\theta_i,\phi_i)\frac{e^{ik_0R}}{R}, \qquad (13)$$

on the initial spherical surface. $C(k_0)$ is a complex energy-dependent coefficient and $Y_{lm}(\theta_i,\phi_i)$ is a spherical harmonic function representing the initial angular distribution of the generated photoelectron wave. For instance, H^- and F^- considered in this work represent a p-wave source and an s-wave source, respectively. The semiclassical wave corresponding to

each trajectory can be written as [17,23]

$$\psi_\nu(t) = f_L(t_i)\psi_{\rm out}(R,\theta_i,\phi_i)\mathcal{A}_\nu e^{i(\mathcal{S}_\nu - E_0 t_i - \lambda_\nu \frac{\pi}{2})}, \tag{14}$$

where the subscript ν labels the considered trajectory. $\mathcal{A}$ and $\mathcal{S}$ denote, respectively, the semiclassical amplitude and classical action accumulated in an augmented phase space. The Maslov index λ is determined by the number of singularities in $\mathcal{A}$ along the trajectory.

When the electron wave returns back to the source region, the returning wave behaves approximately like a plane wave [14,15], traveling along the returning direction of the closed classical orbit. Therefore, by connecting the semiclassical wave in Eq. (14) to a plane-wave form, the electron returning wave along each closed orbit can be approximated as

$$\psi^\nu_{\rm ret}(t) = f_L(t_i)e^{-iE_0 t}\widetilde{\psi}^\nu_{\rm ret}, \tag{15}$$

with the reduced function $\widetilde{\psi}^\nu_{\rm ret}$ specifically expressed as

$$\widetilde{\psi}^{\rm I}_{\rm ret} = C(k_0)\mathcal{G}_{\rm co}Y_{lm}(\theta_i = 0)e^{-ik_{\rm ret}z}, \tag{16}$$

$$\widetilde{\psi}^{\rm II}_{\rm ret} = C(k_0)\mathcal{G}_{\rm co}Y_{lm}(\theta_i = 0)e^{ik_{\rm ret}z}, \tag{17}$$

$$\widetilde{\psi}^{\rm III}_{\rm ret} = C(k_0)\mathcal{G}_{\rm co}Y_{lm}(\theta_i = \pi)e^{ik_{\rm ret}z}, \tag{18}$$

for the wave parts returned along the three types of closed orbits as in Fig. 3(a), respectively. Note that the returning electron momentum $k_{\rm ret}$ in Eqs. (16)–(18) is generally different from the initial momentum k_0 when a time-dependent electric field is applied, which is different from the case of a static field. In the above equations,

$$Y_{lm}(\theta_i = \pi) = (-1)^l Y_{lm}(\theta_i = 0) = (-1)^l N_{l0}\delta_{m0}, \tag{19}$$

with $N_{l0} = \sqrt{(2l+1)/(4\pi)}$, and the factor

$$\mathcal{G}_{\rm co} = \frac{\mathcal{A}}{R}e^{i(\widetilde{\mathcal{S}} - \lambda\frac{\pi}{2})} \tag{20}$$

represents the wave amplitude and phase accumulated along each closed orbit. The redefined action function $\widetilde{\mathcal{S}}$ in Eq. (20) has the following form:

$$\widetilde{\mathcal{S}} = \mathcal{S} + E_0(t - t_i), \tag{21}$$

which is called an "extended action" in Ref. [17].

The general expressions for the semiclassical amplitude $\mathcal{A}$ and classical action $\mathcal{S}$ have been obtained in Ref. [23] for the electron wave propagating along any classical trajectories in a time-dependent external field. For the closed classical orbits involved here, we have

$$\frac{\mathcal{A}}{R} = \frac{1}{k_0(t - t_i)}\left|\frac{k_0}{k_0 - F(t_i)(t - t_i)\cos(\theta_i)}\right|^{1/2} \tag{22}$$

from Eq. (28) in Ref. [23] with $\theta_i = 0$ or π, which can be rewritten as an intuitive form (Appendix A),

$$\frac{\mathcal{A}}{R} = \frac{1}{k_0(t - t_i)}\left|\frac{p_z(t_i)dt_i}{p_z(t)dt}\right|^{1/2}, \tag{23}$$

with $p_z(t_i)$ and $p_z(t)$ denoting, respectively, the outgoing and returning momenta of the corresponding closed orbit. Note that the absolute-square-root part on the right-hand side of Eqs. (22) and (23) becomes a unity when the energy is conserved, and Eqs. (22) and (23) reduce to a static-field case as in [14,15].

Based on Eq. (23), the Maslov index λ can be determined from the returning-time plot as in Fig. 3(a). For example, if $\theta_{\rm ret} = \theta_i = 0$ as the second type of closed orbit in Eq. (17), $\lambda = 0$ when the slope dt/dt_i in Fig. 3(a) is positive, otherwise $\lambda = 1$. From Eq. (B9) in Ref. [23], the extended action $\widetilde{\mathcal{S}}$ in Eq. (36) can be obtained as (Appendix A)

$$\widetilde{\mathcal{S}} = \left[k_0^2 + \frac{1}{2}A^2(t_i) - A(t_i)k_0\cos(\theta_i)\right](t - t_i) - \frac{1}{2}\int_{t_i}^{t} A^2(t')dt' \tag{24}$$

by using the condition in Eq. (8) for a trajectory returning back to the source region.

V. CLOSED-ORBIT THEORY

Following the general picture established in Refs. [3–5,17], the total photodetachment rate $\Upsilon(t)$ in Eq. (5) can be decomposed as

$$\Upsilon(t) = \Upsilon_0(t) + \sum_\nu \Upsilon_\nu(t), \tag{25}$$

where

$$\Upsilon_0(t) = -2{\rm Im}\langle I(t)|\psi_{\rm dir}(t)\rangle \tag{26}$$

is a smooth background representing the photodetachment rate without any external fields, and

$$\Upsilon_\nu(t) = -2{\rm Im}\langle I(t)|\psi^\nu_{\rm ret}(t)\rangle \tag{27}$$

is contributed by the returning electron wave $\psi^\nu_{\rm ret}(t)$ associated with the νth closed orbit. The wave-source function $I(t)$ in Eqs. (26) and (27) has the following form:

$$I(t) = f_L(t)e^{-iE_0 t}D\varphi_i, \tag{28}$$

which is the source term on the right-hand side of Eq. (4) multiplied by a phase term $\exp(-iE_0 t)$. The smooth background in Eq. (26) can be worked out as

$$\Upsilon_0(t) = f_L^2(t)k_0|C(k_0)|^2 \tag{29}$$

according to the existing formulas in Ref. [15] after, in Eq. (26), using the directly outgoing wave $\psi_{\rm dir}(t)$ given by Eq. (2) and the wave-source function $I(t)$ in Eq. (28).

To calculate the contributed term from the returning electron wave, we first rewrite Eq. (27) as

$$\Upsilon_\nu(t) = -2f_L(t)f_L(t_i){\rm Im}\langle D\varphi_i|\widetilde{\psi}^\nu_{\rm ret}\rangle, \tag{30}$$

using the expressions of the returning wave in Eq. (15) and the wave-source function in Eq. (28). The overlap integration in Eq. (30) between a static wave source $D\varphi_i$ and a reduced returning wave $\widetilde{\psi}^\nu_{\rm ret}$ is now in a familiar form usually encountered when a static field is applied. Accordingly, the same manipulations as in Ref. [15] can be followed, and the final expression is (Appendix B)

$${\rm Im}\langle D\varphi_i|\widetilde{\psi}^\nu_{\rm ret}\rangle = \frac{{\rm g}^l}{2}(2l+1)\delta_{m0}{\rm Im}[C^*(k_0)C(k_{\rm ret})\mathcal{G}^*_{\rm co}], \tag{31}$$

with ${\rm g} = 1$ for a closed orbit with the same outgoing and returning directions as in Eq. (17), and ${\rm g} = -1$ for a closed orbit with opposite outgoing and returning directions as in

Eqs. (16) and (18). Therefore, the sinusoidal term $\Upsilon_\nu(t)$ in Eq. (25) corresponding to each closed orbit is obtained as

$$\Upsilon_\nu(t) = \mathrm{g}^l f_L(t) f_L(t_i)(2l+1)\delta_{m0} \times C^*(k_0)C(k_{\rm ret})\frac{\mathcal{A}}{R}\sin\left(\widetilde{\mathcal{S}} - \lambda\frac{\pi}{2}\right), \quad (32)$$

by substituting Eq. (31) into Eq. (30). To write Eq. (32), we have assumed that the energy-dependent coefficient $C(k)$ is either a real function or a pure imaginary function, as discussed in Refs. [36,37].

Finally, the closed-form expression for the photodetachment rate can be written as a product,

$$\Upsilon(t) = \Upsilon_c \mathcal{H}(t), \quad (33)$$

by combining Eqs. (25), (29), and (32) together, where

$$\Upsilon_c = k_0 |C(k_0)|^2 \quad (34)$$

represents the photodetachment rate in a weak cw laser field with $f_L(t) = 1$, and

$$\mathcal{H}(t) = f_L^2(t) + \sum_\nu f_L(t) f_L(t_i^\nu)\mathcal{H}^\nu(t) \quad (35)$$

contains both the possible effects induced by an external field and the slowly varying envelope $f_L(t)$ assumed for the weak laser field. In the summation of Eq. (35), one of the laser-field envelope functions $f_L(t)$ is evaluated at t_i, which was brought in by the initially outgoing wave in Eq. (2) through the returning wave in Eq. (15). The presence of the prefactor $f_L(t)f_L(t_i)$ in Eq. (35) requires the occurrence of the laser excitations at both the instant t_i and t, as well as a quantum coherence between these two excitation events. $\mathcal{H}(t)$ in Eq. (35) is usually called a modulation function of the photodetachment rate, and $\mathcal{H}^\nu(t)$ corresponds to the contribution from each closed orbit, which can be explicitly written as

$$\mathcal{H}^\nu(t) = \mathrm{g}^l(2l+1)\delta_{m0}\frac{C(k_{\rm ret})}{C(k_0)}\frac{\mathcal{A}}{k_0 R}\sin\left(\widetilde{\mathcal{S}} - \lambda\frac{\pi}{2}\right) \quad (36)$$

from Eqs. (32)–(35). Required by a Wigner power law such as $\Upsilon_c \propto (k_0)^{2l+1}$ near the photodetachment threshold [38], the energy-dependent coefficient $C(k)$ is proportional to k^l for small k. For H^- especially, an analytic form of $C(k)$ needed in Eq. (36) has been given by a well-established model in Refs. [26,39], and

$$\frac{C(k_{\rm ret})}{C(k_0)} = \frac{k_{\rm ret}(E_b + E_0)^2}{k_0(E_b + E_{\rm ret})^2}, \quad (37)$$

with $E_{\rm ret} = k_{\rm ret}^2/2$. For $E_0 \ll E_b$ and $E_{\rm ret} \ll E_b$, Eq. (37) reduces to that given by the Wigner threshold law.

At the end of this section, we would like to point out that no specific profile has been assumed for the applied electric field in the above derivation. All of the formulas obtained in this section are generally applicable for the photodetachment in a time-dependent electric field oscillating at low frequency, which automatically includes the static-field case as in Refs. [14,15]. Since the semiclassical propagation scheme and its related formulas in Ref. [23] were also presented in a general form for the electron propagating along any classical trajectories, the established theory, together with Ref. [23], provides an intuitive understanding of the photodetachment dynamics driven by a slowly varying oscillating electric field, which depicts a clear dynamical picture from a time-dependent viewpoint based on the classical trajectory propagation.

VI. CALCULATIONS AND DISCUSSIONS

In this section, we present some specific calculations using Eqs. (35) and (36) for the photodetachment driven by a single-cycle THz pulse as illustrated in Fig. 1(a), as well as the related discussions on the possible interesting effects expected from the current theory. The exact quantum simulations are also presented for several cases to examine the accuracy of the simple formulas in Eqs. (35) and (36). For H^- as a p-wave source, the expression in Eq. (37) is used. For F^- as an s-wave source, we consistently use $C(k_{\rm ret})/C(k_0) = 1$ after the Wigner power law near the photodetachment threshold.

The photodetachment rate given by the generalized closed-orbit theory is compared with that from exact quantum simulations in Fig. 3(b) by taking the demonstrated case in Fig. 1(b), for instance. Excellent agreement can be found in the time range where the electron can be classically driven back to the source region. Near the classical boundary corresponding to the left-most points of the solid blue line and the dashed black curve in Fig. 3(a), the results from closed-orbit theory diverge as usual because $dt/dt_i = 0$ in the semiclassical amplitude as in Eq. (23). Besides, as shown by the quantum simulations in Figs. 3–5, the oscillatory behavior of the photodetachment rate can also be observed in the classically forbidden range where no closed classical orbit was found, and the oscillation amplitude goes to zero gradually with time t away from the classical boundary.

The above-mentioned oscillation behavior in the classically forbidden region looks similar to that observed in Ref. [40] for a static barrier, where the continuation of the cross-section oscillations beyond the standard closed-orbit theory was explained as an effect of quantum over-barrier reflection. However, our current time-dependent system is more complicated than the static case in Ref. [40]. To quantitatively describe those extended oscillations in the classically forbidden region, as well as to repair the divergence near the classical boundary as in Fig. 3(b), some sophisticated manipulations are needed beyond our current treatment based on real classical trajectories [11,15,40]. Nevertheless, the semiclassical formulas obtained in Sec. V are already insightful enough to understand the physics behind the complicated oscillations of the photodetachment rate as in Fig. 1(b). Therefore, in the following discussion, we will mainly focus on the physics revealed by Eqs. (35) and (36), instead of pursuing an appropriate way to save the semiclassical description near the classical boundary and in the classically forbidden region. In addition, it can be seen from Figs. 3–5 that quantum effects in the classically forbidden region become negligible when the THz pulse gets stronger relative to the initial electron kinetic energy.

Beyond the specific case of H^-, the established theory in Sec. V promises an interesting discrepancy between the oscillation behaviors of the photodetachment rates for different negative ions. To give a general impression, the photodetachment rate for F^- is also displayed in Fig. 3(c) from quantum calculations, where both the oscillation amplitude and phase

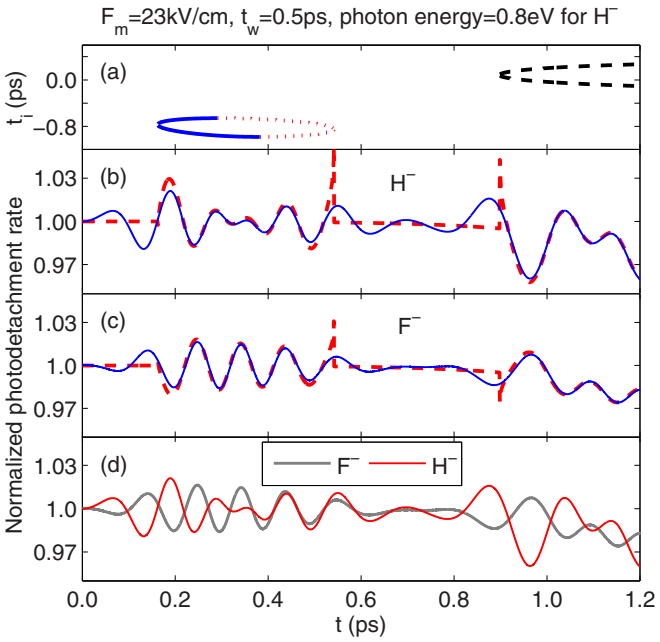

FIG. 4. Phase dependence on a simple geometry of the closed orbit. (a) Returning time plot for the relevant closed orbits. The solid blue curve and the dotted and the dashed lines correspond to the closed orbits with ($\theta_i = 0$, $\theta_{\rm ret} = \pi$), $\theta_i = \theta_{\rm ret} = 0$, and ($\theta_i = \pi$, $\theta_{\rm ret} = 0$), respectively. (b),(c) The time-dependent photodetachment rate for H^- and F^-, respectively. The bold dashed and the solid blue curves are given by closed-orbit theory and quantum simulations, respectively. (d) Comparison between the photodetachment rates for H^- (thin red curve) and F^- (bold gray line) obtained from quantum simulations. All of the quantum results have been normalized using the value of the photodetachment rate at $t = 0$ ps without any external fields applied.

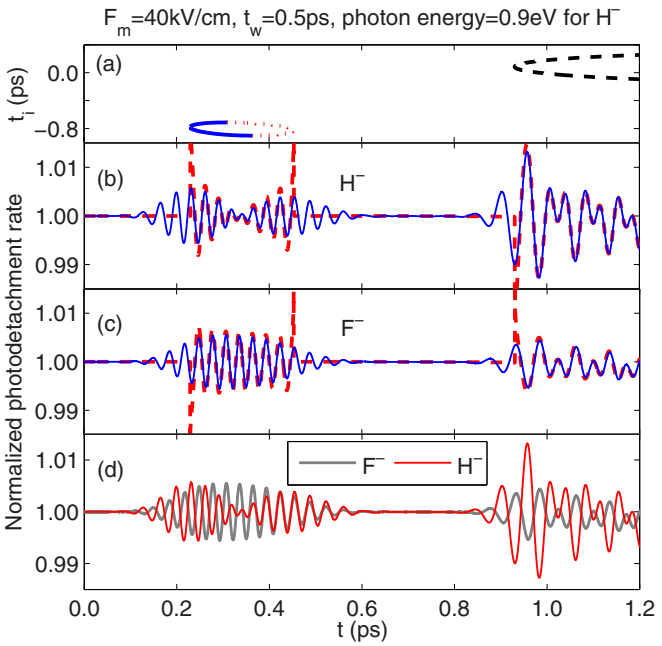

FIG. 5. The same as Fig. 4, but for higher photon energy and larger field strength as listed on the top. Here, t_L in Eq. (1) was set to be $50T_0$ as in Ref. [23].

are very different from those observed for H^-. Since the oscillations in Fig. 3 are too complicated to give any clear information, we choose to first examine the two simpler cases in Figs. 4 and 5, where the time ranges corresponding to the three types of closed orbits are almost separated between each other, supported qualitatively by the graphic analysis as in Fig. 2 with Eqs. (9) and (10) together. Comparing with those parameters in Fig. 3, the field strength is smaller in Fig. 4, while the photon energy is higher in Fig. 5. For both of the two cases in Figs. 4 and 5, a good agreement between closed-orbit theory and quantum calculations can also be found in the classically allowed range for closed classical orbits. By comparing H^- and F^- in each case, as in Figs. 4(d) and 5(d), different phase relations can be observed in different time ranges for the oscillations of the photodetachment rates.

According to Eq. (36) for each specific closed orbit, the modulation phase for different negative ions is only determined by a g coefficient associated with a simple geometry of the closed orbit. If the contributed closed orbit has the opposite outgoing and returning directions as those identified by the solid and the dashed curves in Figs. 3(a), 4(a), and 5(a), the prefactor g^l can be 1 or -1, depending on whether the quantum number l is even or odd. Therefore, the photodetachment rate for H^- (p-wave source) oscillates out of phase with that for F^- (s-wave source) in the corresponding time ranges. In contrast, if the outgoing and returning directions of the closed orbit are the same as the second type of closed orbit indicated by the dotted lines in Figs. 3(a), 4(a), and 5(a), then the prefactor $g^l = 1$ for all l values. Accordingly, the photodetachment rates for H^- and F^- oscillate in phase in the time range of the second type of closed orbit. These arguments based on the g coefficient in Eq. (36) successfully explain the different phase relations between the oscillatory curves for H^- and F^- in the different time ranges of Figs. 4(d) and 5(d).

More interestingly, near $t \sim 0.3$ ps in both Figs. 4 and 5 where time ranges for the first and second types of closed orbits overlap, the oscillation amplitude of the photodetachment rate for H^- becomes smaller but the amplitude for F^- gets larger. This is also caused by the g coefficient. For H^-, $g^l = -1$ and 1 for the first and second types of closed orbits, respectively. Therefore, the total contributions from these two closed orbits at each time become smaller because of a large-part cancellation between each other in Eq. (35). For F^-, both types of closed orbits have $g^l = 1$, and accordingly their incoherent summation in Eq. (35) makes the oscillation amplitude larger. Nevertheless, the same phenomenon does not appear in Fig. 3(c), which cannot be simply explained by the g coefficient. Note that the closed orbits starting near $t_i = -2$ ps need a much longer time to be driven back to the source region than those starting near $t_i = 0$ ps do. Consequently, their contributions in Eq. (35) are negligible compared with those contributed by the closed orbits starting much later, as a result of their associated much weaker amplitudes $\mathcal{A}$ according to Eq. (22). This can be seen clearly in the overlap range near $t = 0.4$ ps in Fig. 3(c), where the oscillation behavior is dominated by the second type of closed orbit, and the photodetachment rates for H^- and F^- oscillate in phase.

Following Eq. (36), the modulation amplitude is generally affected by both the energy-dependent coefficient $C(k)$ and the angular distribution of an initially outgoing wave. Specifically,

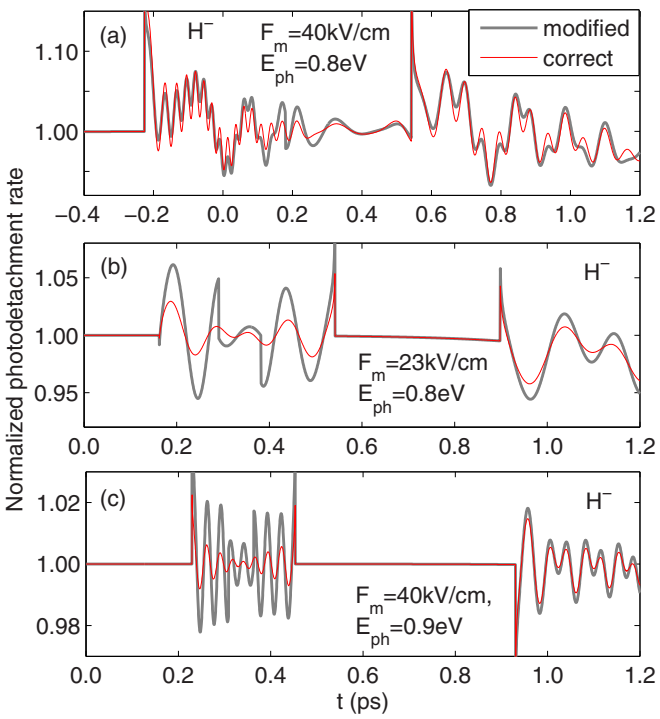

FIG. 6. Amplitude dependence on the returning electron momentum for H^-. The thin solid (red) curves in (a)–(c) are reproduced from the bold dashed lines in Figs. 3(b), 4(b), and 5(b), respectively, for comparison. The bold gray lines are calculated from Eq. (36) without the term $C(k_{\rm ret})/C(k_0)$ included.

for an s-wave source such as F^-, the effect of $C(k)$ is negligible according to the Wigner power law near the photodetachment threshold. However, for a p-wave source such as H^-, the effect of $C(k)$ is not negligible in principle according to Eqs. (36) and (37), and the change of the electron returning momentum $k_{\rm ret}$ relative to the initially outgoing momentum k_0 might modify the oscillation amplitude of the photodetachment rate dramatically. As a demonstration, the correct semiclassical results in Figs. 3(b), 4(b), and 5(b) are compared in Figs. 6(a)–6(c), respectively, with their modified calculations according to Eq. (36) without the term $C(k_{\rm ret})/C(k_0)$ included. Note that the modified results give an oscillation amplitude only determined by the factor $(2l+1)$ in Eqs. (35) and (36) for the same types of closed orbits. By comparing Figs. 6(a)–6(c) and Figs. 3(c), 4(d), and 5(d) correspondingly, we can conclude that the oscillation-amplitude discrepancy between the photodetachment rates for H^- and F^- in Fig. 3(c) is mainly caused by the different l values associated with the wave-source property, while the almost equal oscillation amplitudes observed in both Figs. 4(d) and 5(d) are induced by the change of the returning momentum related to the external time-dependent field.

A dynamic picture of the electron-momentum variation and also the difference between $k_{\rm ret}$ and k_0 can be obtained visually from a graphic demonstration of Eq. (8) as in Fig. 2. The vertical vector from the reverted vector-potential curve to the horizontal dashed line as in Fig. 2(a) is just the electron momentum vector at each time instant. The specific case illustrated in Fig. 2 corresponds to Figs. 3 and 6(a). There is no big difference observed between $k_{\rm ret}$ and k_0 in Fig. 2 for most cases, especially for the first-time returning orbit in Fig. 2(a) and those closed orbits as in Fig. 2(g) which contribute dominantly to the final oscillation amplitude because of their short durations. This explains the small discrepancy between the modified results and the correct calculations in Fig. 6(a). Besides the overall agreement, an obvious discrepancy can be found near $t = 0.2$ ps in Fig. 6(a). This is because the electron experiences a soft return as in Fig. 2(c) where the returning momentum is zero. Accordingly, as shown in Fig. 6(a), the oscillation amplitude from correct calculations appears smaller than that given by the modified results without the term $C(k_{\rm ret})/C(k_0)$ included in Eq. (36).

There are mainly three differences between the cases in Figs. 6(b) and 6(c) and that in Fig. 6(a). First, all of the closed orbits almost contribute equally to the oscillation amplitudes in Figs. 6(b) and 6(c) as a result of their similar durations. Second, compared with those parameters in Fig. 6(a), the field strength is weaker in Fig. 6(b) and the photon energy is higher in Fig. 6(c). If we make a corresponding change in Fig. 2 after Fig. 4(a) or Fig. 5(a), the obtained returning momenta are almost always smaller than the initial values. This is the main reason why the modified results give a larger amplitude than the correct calculations in Figs. 6(b) and 6(c). The third important difference is that the time range for the first and second types of closed orbits in Figs. 4(a) and 5(a) is much more localized near the time instant of a soft return than that in Fig. 3(a). This is another origin for the large discrepancy observed near $t \sim 0.4$ ps in Figs. 6(b) and 6(c). An additional interesting effect related to the soft return is the discontinuity of the modified results as in Fig. 6, which is caused by the sign change of g^l on the two sides of the softly returning time.

Another interesting aspect related to our present work is about the static-field approximation in a long-wavelength limit of the applied oscillating field. As introduced in Sec. I, it has been found that the static-field approximation for each photodetachment event works very well for an experiment in a strong microwave field [28,29]. Our current theory has already allowed us to examine this simple quasistatic picture from a time-dependent viewpoint. For this purpose, we take H^-, for instance, and compare the time-dependent photodetachment rate given by Eq. (35) with the quasistatic result obtained from [14,15],

$$\mathcal{H}^F(t) = f_L^2(t)\left[1 + \frac{1}{\mathcal{S}_F}\cos(\mathcal{S}_F)\delta_{m0}\right], \tag{38}$$

where $\mathcal{S}_F = 4\sqrt{2}E_0^{3/2}/(3|F(t)|)$ denotes the classical action of an electron returned back to the source region along the unique closed orbit in a static electric field. Some specific calculations are shown in Figs. 7 and 8 by varying the single-cycle pulse duration and strength, respectively. It can be found that the time-dependent calculations indeed approximate the quasistatic results gradually when the field oscillation period gets longer or the field strength becomes larger. The agreement observed in Figs. 7 and 8 is best near the field peak position and worst near the zero-field locations. However, the contribution in the time-averaged observations mainly comes from the oscillations near the field peak position because both the

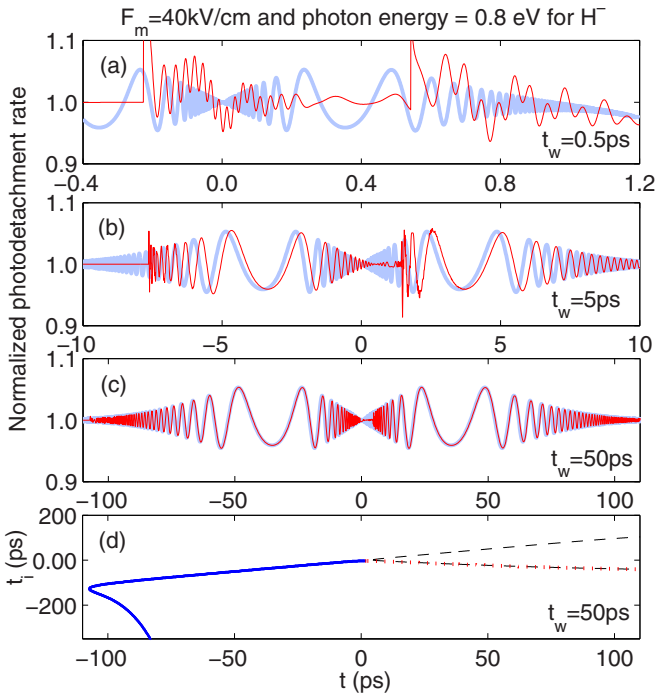

FIG. 7. (a)–(c) Comparison between the time-dependent calculations from Eq. (35) (heavy thin curves) and a static-field approximation after Eq. (38) (light bold lines) by increasing the single-cycle pulse duration. (d) The returning time plot for the relevant closed orbits in (c). The solid blue curve and the dotted and dashed lines correspond to the closed orbits with ($\theta_i = 0$, $\theta_{\rm ret} = \pi$), $\theta_i = \theta_{\rm ret} = 0$, and ($\theta_i = \pi$, $\theta_{\rm ret} = 0$), respectively.

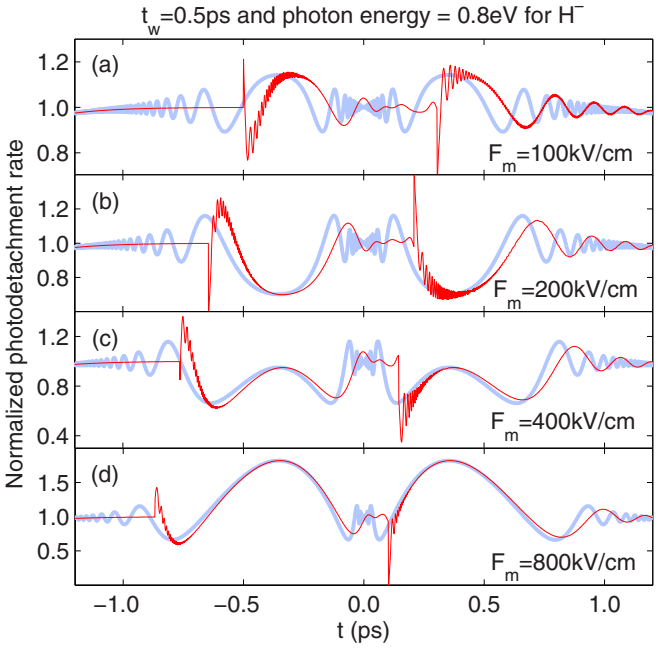

FIG. 8. Comparison between the time-dependent calculations from Eq. (35) (heavy thin curves) and a static-field approximation after Eq. (38) (light bold lines) by increasing the single-cycle pulse strength.

oscillation amplitude and period near the zero-field locations are too small to give a finite averaged signal, which confirms the validity of the static-field approximation used before. In Fig. 7(d), the returning-time plot is given for the relevant closed orbits in Fig. 7(c), which illustrates the physics behind the agreement observed in Figs. 7 and 8. Although the three types of closed orbits as in Fig. 2 are all there, only those closed orbits located near the line $t = t_i$ in Fig. 7(d) have an observable effect in the oscillation amplitude of the photodetachment rate because their durations $t - t_i$ are much shorter than the others, and the associated returning-wave amplitudes $\mathcal{A}$ in Eqs. (22) and (23) are large enough.

VII. CONCLUSION

Motivated by our recent studies on the temporal interferences in the photodetachment of negative ions driven by a single-cycle THz pulse [23], we examined the possible influences of a single-cycle THz pulse on the time-dependent photodetachment rate. We found that a weak THz pulse cannot change the total photodetachment rate. However, if the applied THz pulse gets strong enough, the photodetachment rate oscillates complicatedly. On the other hand, we noticed that some classical trajectories of the photoelectron can be driven back to the source region by a strong single-cycle THz pulse. These observations remind us of a general picture already recognized in the standard closed-orbit theory [3–5], which addresses the correspondence between the oscillatory photoionization (or photodetachment) rate and the possible closed classical orbits embedded in the system.

To quantitatively understand the complex structures observed in the time-dependent photodetachment rate, the standard closed-orbit theory for the photodetachment in a static electric field has been generalized to a time-dependent form which agrees well with exact quantum simulations. The established formulas reveal a simple dependence of the photodetachment-rate oscillations on the properties of both the wave source and the closed classical orbits existing in the system. Depending on the relative direction of the returning orbit with respect to its initially outgoing direction, the photodetachment rates for different negative ions such as H^- and F^- might oscillate in phase or out of phase. In contrast to the case of a static electric field [14,15], the oscillation amplitude of the photodetachment rate contributed by each closed orbit has an additional term determined by the electron returning momentum which is usually different from the initially outgoing momentum. As the applied electric field gets stronger or its oscillation period becomes longer, the oscillatory behavior of the photodetachment rate is more and more like that obtained from the static-field approximation as in Refs. [28,29].

The presented theory provides a clear and intuitive picture for the photodetachment dynamics driven by a general time-dependent electric field. Benefiting from the correlation between the electron launch time and its later-returning time, a similar pump-probe technique as in Ref. [41] may be a possible candidate in future experiments for exploring the quantum effect of closed classical orbits from a time-dependent viewpoint. An immediate application of the current theory would be the photodetachment of negative ions in a static electric

field plus a strong oscillating electric field, where the averaged photodetachment rate can be detected as in Ref. [16]. For a weak oscillating field, the perturbation formulas in Ref. [17] can be used. More interesting physics can be expected when the oscillating field amplitude is comparable to or even larger than the static field strength, which is also an interesting topic for future studies.

ACKNOWLEDGMENTS

B.C.Y. thanks George Simion for helpful discussions. This work was supported by the U.S. Department of Energy, Office of Science, Basic Energy Sciences, under Award No. DE-SC0012193. This research was supported in part through computational resources provided by Information Technology at Purdue University, West Lafayette, Indiana.

APPENDIX A: THE DERIVATION OF EQS. (23) AND (24)

The electron motion equation can be formally written as

$$\rho = \rho(t_i,\theta_i,t) \text{ and } z = z(t_i,\theta_i,t) \tag{A1}$$

in the cylindric-coordinate frame. If we fix the electron final destination (ρ, z) but let the other parameters change, the following partial differential equation can be obtained:

$$\left(\frac{\partial\rho}{\partial t}\right)_{t_i,\theta_i}\left(\frac{\partial t}{\partial t_i}\right)_{\rho,z} + \left(\frac{\partial\rho}{\partial\theta_i}\right)_{t_i,t}\left(\frac{\partial\theta_i}{\partial t_i}\right)_{\rho,z} = -\left(\frac{\partial\rho}{\partial t_i}\right)_{t,\theta_i}, \tag{A2}$$

which can be explicitly written as

$$\sin\theta_i\left(\frac{\partial t}{\partial t_i}\right)_{\rho,z} + (t-t_i)\cos\theta_i\left(\frac{\partial\theta_i}{\partial t_i}\right)_{\rho,z} = \sin\theta_i \tag{A3}$$

using Eq. (6). Similarly, we have

$$[k_0\cos\theta_i + A(t) - A(t_i)]\left(\frac{\partial t}{\partial t_i}\right)_{\rho,z} - k_0(t-t_i)\sin\theta_i \times\left(\frac{\partial\theta_i}{\partial t_i}\right)_{\rho,z} = k_0\cos\theta_i - F(t_i)(t-t_i) \tag{A4}$$

from Eq. (7). After eliminating the partial derivative $(\frac{\partial\theta_i}{\partial t_i})_{\rho,z}$ in Eqs. (A3) and (A4), we get

$$\left(\frac{\partial t}{\partial t_i}\right)_{\rho,z} = \frac{k_0 - F(t_i)(t-t_i)\cos\theta_i}{k_0 + [A(t) - A(t_i)]\cos\theta_i}. \tag{A5}$$

For the closed orbits returning back to the atom center, the partial derivative $(\frac{\partial t}{\partial t_i})_{\rho,z}$ becomes dt/dt_i, and Eq. (23) is obtained by combining Eqs. (A5) and (22) and also using $p_z(t) = k_0\cos\theta_i + A(t) - A(t_i)$ with $\theta_i = 0$ or π.

The classical action $\mathcal{S}$ along an arbitrary trajectory has been obtained as [23]

$$\mathcal{S} = E_0(t-t_i) + z(t)\Delta p_z(t) - \frac{1}{2}\int_{t_i}^{t}[\Delta p_z(t')]^2dt', \tag{A6}$$

with the momentum transfer

$$\Delta p_z(t) = A(t) - A(t_i). \tag{A7}$$

For the closed orbits, $z(t) = 0$, and the action $\mathcal{S}$ can be unfolded as

$$\mathcal{S} = E_0(t-t_i) - \frac{1}{2}A^2(t_i)(t-t_i) + A(t_i)\int_{t_i}^{t}A(t')dt' - \frac{1}{2}\int_{t_i}^{t}[A(t')]^2dt', \tag{A8}$$

by substituting Eq. (A7) into the last integration in Eq. (A6). The closed-orbit condition in Eq. (8) allows the above equation to be further simplified as

$$\mathcal{S} = \left[E_0 + \frac{1}{2}A^2(t_i) - A(t_i)k_0\cos\theta_i\right](t-t_i) - \frac{1}{2}\int_{t_i}^{t}A^2(t')dt', \tag{A9}$$

which gives Eq. (24) after the definition in Eq. (21).

APPENDIX B: THE DERIVATION OF EQ. (31)

To be clear, we write the oscillatory term $\Upsilon_v(t)$ in Eq. (30) as the following form:

$$\Upsilon_{\pm z}(t) = -2f_L(t)f_L(t_i)\mathrm{Im}\langle D\varphi_i|\widetilde{\psi}_{\mathrm{ret}}^{(\pm z)}\rangle, \tag{B1}$$

where the notation $\pm z$ is used to indicate the returning direction of the closed orbit. Specifically,

$$\widetilde{\psi}_{\mathrm{ret}}^{(+z)} = C(k_0)\mathcal{G}_{\mathrm{co}}Y_{lm}(\theta_i,\phi_i)e^{ik_{\mathrm{ret}}z}, \tag{B2}$$

representing the returning electron wave along the positive-z direction, and

$$\widetilde{\psi}_{\mathrm{ret}}^{(-z)} = C(k_0)\mathcal{G}_{\mathrm{co}}Y_{lm}(\theta_i,\phi_i)e^{-ik_{\mathrm{ret}}z}, \tag{B3}$$

denoting the returning wave along the negative-z direction. In both Eqs. (B2) and (B3), θ_i can be 0 or π, and the complex term $\mathcal{G}_{\mathrm{co}}$ is given by Eq. (20).

The overlap integration $\langle D\varphi_i|\widetilde{\psi}_{\mathrm{ret}}^{(\pm z)}\rangle$ in Eq. (B1) has almost the same form as that studied in Ref. [15], except that the electron returning momentum k_{ret} is not conserved in our current system. On the other hand, we note that the inhomogeneous Schrödinger equation,

$$\left[\frac{1}{2}\nabla^2 + \frac{1}{2}k^2 - V(r)\right]\widetilde{\psi}_{\mathrm{out}}^{(k)} = D\varphi_i, \tag{B4}$$

should be valid for any values of the momenta k, where the related outgoing wave $\widetilde{\psi}_{\mathrm{out}}^{(k)}$ has the same asymptotic form as in Eq. (13) but with a different momentum value. Therefore, the same idea used in Appendix A of Ref. [15] can also be implemented, and the imaginary part of the overlap integration in Eq. (B1) can be converted to

$$\mathrm{Im}\langle D\varphi_i|\widetilde{\psi}_{\mathrm{ret}}\rangle = \frac{1}{2}\mathrm{Im}\int(\widetilde{\psi}_{\mathrm{out}}\nabla_r\widetilde{\psi}_{\mathrm{ret}}^{*} - \widetilde{\psi}_{\mathrm{ret}}^{*}\nabla_r\widetilde{\psi}_{\mathrm{out}})ds_r, \tag{B5}$$

after replacing the source term $D\varphi_i$ by the outgoing wave function $\widetilde{\psi}_{\mathrm{out}}^{(k_{\mathrm{ret}})}$ with $k = k_{\mathrm{ret}}$ in Eq. (B4). The integration in Eq. (B5) is on a spherical surface with a radius r centered at the negative ion.

Following Appendix B in Ref. [15], the two relevant integrations in Eq. (B5) can be worked out as

$$\int \widetilde{\psi}_{\rm out} \nabla_r \left[\widetilde{\psi}_{\rm ret}^{(\pm z)}\right]^* ds_r = \frac{1}{2}(\pm 1)^l \mathcal{C}_{lm}\sqrt{4\pi(2l+1)}\left[1+e^{i(2k_{\rm ret}r-l\pi)}\right]\delta_{m0} \tag{B6}$$

and

$$\int \left[\widetilde{\psi}_{\rm ret}^{(\pm z)}\right]^* \nabla_r \widetilde{\psi}_{\rm out} ds_r = -\frac{1}{2}(\pm 1)^l \mathcal{C}_{lm}\sqrt{4\pi(2l+1)}[1-e^{i(2k_{\rm ret}r-l\pi)}]\delta_{m0}, \tag{B7}$$

where

$$\mathcal{C}_{lm} = C(k_{\rm ret})C^*(k_0)\mathcal{G}_{\rm co}^* Y_{lm}^*(\theta_i,\phi_i). \tag{B8}$$

The expression in Eq. (31) is obtained by substituting Eqs. (B6) and (B7) into Eq. (B5) with Eqs. (B8) and (19) together. Note that the r-dependent terms in Eqs. (B6) and (B7) cancel each other.

[1] M. C. Gutzwiller, *Chaos in Classical and Quantum Mechanics* (Springer-Verlag, New York, 1990).
[2] D. Kleppner and J. B. Delos, Found. Phys. **31**, 593 (2001), and references therein.
[3] M. L. Du and J. B. Delos, Phys. Rev. Lett. **58**, 1731 (1987).
[4] M. L. Du and J. B. Delos, Phys. Rev. A **38**, 1896 (1988).
[5] M. L. Du and J. B. Delos, Phys. Rev. A **38**, 1913 (1988).
[6] J. Gao, J. B. Delos, and M. Baruch, Phys. Rev. A **46**, 1449 (1992).
[7] J. Gao and J. B. Delos, Phys. Rev. A **46**, 1455 (1992).
[8] A. D. Peters and J. B. Delos, Phys. Rev. A **47**, 3020 (1993).
[9] A. D. Peters, C. Jaffé, and J. B. Delos, Phys. Rev. A **56**, 331 (1997).
[10] J. Main, G. Wiebusch, K. Welge, J. Shaw, and J. B. Delos, Phys. Rev. A **49**, 847 (1994).
[11] J. Main and G. Wunner, Phys. Rev. A **55**, 1743 (1997).
[12] A. Matzkin, P. A. Dando, and T. S. Monteiro, Phys. Rev. A **66**, 013410 (2002).
[13] J. D. Wright, J. M. DiSciacca, J. M. Lambert, and T. J. Morgan, Phys. Rev. A **81**, 063409 (2010).
[14] M. L. Du, Phys. Rev. A **70**, 055402 (2004).
[15] B. C. Yang, J. B. Delos, and M. L. Du, Phys. Rev. A **89**, 013417 (2014).
[16] N. Spellmeyer, D. Kleppner, M. R. Haggerty, V. Kondratovich, J. B. Delos, and J. Gao, Phys. Rev. Lett. **79**, 1650 (1997).
[17] M. R. Haggerty and J. B. Delos, Phys. Rev. A **61**, 053406 (2000).
[18] S. Li and R. R. Jones, Phys. Rev. Lett. **112**, 143006 (2014).
[19] B. C. Yang and F. Robicheaux, Phys. Rev. A **90**, 063413 (2014).
[20] B. C. Yang and F. Robicheaux, Phys. Rev. A **91**, 043407 (2015).
[21] S. Fleischer, Y. Zhou, R. W. Field, and K. A. Nelson, Phys. Rev. Lett. **107**, 163603 (2011).
[22] K. N. Egodapitiya, S. Li, and R. R. Jones, Phys. Rev. Lett. **112**, 103002 (2014).
[23] B. C. Yang and F. Robicheaux, Phys. Rev. A **92**, 063410 (2015).
[24] I. I. Fabrikant, Sov. Phys. JETP **52**, 1045 (1980).
[25] Y. N. Demkov, V. D. Kondratovich, and V. N. Ostrovskii, JETP Lett. **34**, 403 (1981).
[26] M. L. Du, Phys. Rev. A **40**, 4983 (1989).
[27] C. Blondel, C. Delsart, and F. Dulieu, Phys. Rev. Lett. **77**, 3755 (1996).
[28] M. C. Baruch, T. F. Gallagher, and D. J. Larson, Phys. Rev. Lett. **65**, 1336 (1990).
[29] M. C. Baruch, W. G. Sturrus, N. D. Gibson, and D. J. Larson, Phys. Rev. A **45**, 2825 (1992).
[30] A. Bugacov, B. Piraux, M. Pont, and R. Shakeshaft, Phys. Rev. A **45**, 3041 (1992).
[31] S. Bivona, R. Burlon, and C. Leone, Phys. Rev. A **45**, 3268 (1992).
[32] C. Laughlin and Shih-I Chu, Phys. Rev. A **48**, 4654 (1993).
[33] X. X. Zhou, Z. J. Chen, T. Morishita, A. T. Le, and C. D. Lin, Phys. Rev. A **77**, 053410 (2008).
[34] A. Kästner, U. Saalmann, and J. M. Rost, Phys. Rev. Lett. **108**, 033201 (2012).
[35] A. Kästner, U. Saalmann, and J. M. Rost, J. Phys. B **45**, 074011 (2012).
[36] C. Bracher, T. Kramer, and M. Kleber, Phys. Rev. A **67**, 043601 (2003).
[37] C. Bracher, Ph.D. thesis, Technische Universität München, 1999.
[38] E. P. Wigner, Phys. Rev. **73**, 1002 (1948).
[39] M. L. Du and J. B. Delos, Phys. Rev. A **38**, 5609 (1988).
[40] B .C Yang and M. L. Du, J. Phys. B **45**, 175003 (2012).
[41] T. Remetter, P. Johnsson, J. Mauritsson, K. Varjú, Y. Ni, F. Lépine, E. Gustefsson, M. Kling, J. Khan, R. López-Martens, K. J. Schafer, M. J. J. Vrakking, and A. L'huillier, Nat. Phys. **2**, 323 (2006).